Polarity-Driven Polytypic Branching in Cu-Based Quaternary Chalcogenide Nanostructures

Reza R. Zamani,[†,‡,*] Maria Ibáñez,[‡] Martina Luysberg,[§] Nuria García-Castelló,[⊥] Lothar Houben,[§] Joan Daniel Prades,[⊥] Vincenzo Grillo,[∥,#] Rafal E. Dunin-Borkowski,[§] Joan Ramón Morante,[‡,⊥] Andreu Cabot,[‡,⊗] and Jordi Arbiol[†,⊗,*]

[†]Institut de Ciència de Materials de Barcelona (ICMAB-CSIC), Campus de la UAB, Bellaterra 08193, Spain, [‡]Catalonia Institute for Energy Research (IREC), Jardins de les Dones de Negre 1, Sant Adrià del Besòs, Barcelona 08930, Spain, [§]Ernst Ruska-Centre for Microscopy and Spectroscopy with Electrons, Forschungszentrum Jülich GmbH, Jülich 52425, Germany, [⊥]Departament d'Electrònica, Universitat de Barcelona, Barcelona 08028, Spain, [∥]Centro S3, CNR—Istituto di Nanoscienze, Via Campi 213A, Modena 41125, Italy, [#]IMEM—CNR, Parco Area delle Scienze 37/A, Parma 43010, Italy, and [⊗]Institució Catalana de Recerca i Estudis Avançats (ICREA), Barcelona 08010, Spain

ABSTRACT An appropriate way of realizing property nanoengineering in complex quaternary chalcogenide nanocrystals is presented for $Cu_2Cd_xSnSe_y$(CCTSe) polypods. The pivotal role of the polarity in determining morphology, growth, and the polytypic branching mechanism is demonstrated. Polarity is considered to be responsible for the formation of an initial seed that takes the form of a tetrahedron with four cation-polar facets. Size and shape confinement of the intermediate pentatetrahedral seed is also attributed to polarity, as their external facets are anion-polar. The final polypod extensions also branch out as a result of a cation-polarity-driven mechanism. Aberration-corrected scanning transmission electron microscopy is used to identify stannite cation ordering, while *ab initio* studies are used to show the influence of cation ordering/distortion, stoichiometry, and polytypic structural change on the electronic band structure.

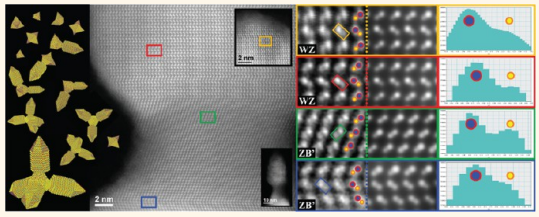

KEYWORDS: wurtzite/zinc-blende polytypes · polarity · $Cu_2CdSnSe_4$ · tetrapod · polytypic branching · cation ordering · electronic band structure

Copper-based chalcogenide semiconductor nanocrystals are used in several energy-related applications due to their suitable optical, electronic, and thermoelectric properties.[1] In particular, ternary and quaternary copper-based chalcogenides offer a broad range of possibilities for morphological, chemical, and structural control through chemical routes, thus providing an opportunity for further functionality enhancement.[2−4] Control of branching, polytypism, polarity, and cation ordering can be independently used to nanoengineer the properties of the material.

Particularly, branching in nanocrystals shows unique influence on the functionality of the compounds,[5] for instance the electronic state.[6,7] Hierarchically organized branched nanostructures find various applications,[8−12] as they provide (i) higher surface area in dye-sensitized solar cells[13] and lithium ion batteries,[14] (ii) self-aligning on a substrate, which introduces direct paths for charge transport between planar electrodes, and/or (iii) epitaxial heterostructures to fabricate nanodevices with efficient contacts at the nanoscale.[15,16]

Branching is intimately related to polytypism.[5,7] In *polytypic branching* generally wurtzite (WZ) extensions of the nanoparticle branch out from a zinc-blende (ZB) seed, as observed in a plethora of binary chalcogenide nanocrystals such as CdS,[17] CdTe,[18,19] and CdSe.[19,20] Even recently Wang *et al.* reported on ternary Cu_2SnSe_3 (CTSe) tetrapods with wurtzite extensions.[21] However, to the best of our knowledge, there is no report on quaternary $Cu_2Cd_xSnSe_y$ (CCTSe) branched nanocrystals or any other quaternary chalcogenides. Polytypism indeed is a phenomenon that regularly takes place in tetrahedrally coordinated semiconductors, especially Si,[22−24] III—V,[25−28] and II—VI[29−31] nanostructures.

* Address correspondence to reza.r.zamani@gmail.com; arbiol@icrea.cat.

Received for review November 5, 2013 and accepted February 27, 2014.

Published online February 27, 2014
10.1021/nn405747h

It has even been observed in ternary and quaternary copper-based chalcogenides.[32] In these materials, the (111) atomic planes of the cubic structure, well known as zinc-blende, are equivalent to the (0001) atomic planes of the hexagonal structure that has a wurtzite structure belonging to the $P6_3mc$ space group. The difference between both crystal phases lies in the different stacking of the atoms along the (111) or (0001) planes, being *abcabc* and *abababab* for zinc-blende and wurtzite, respectively. Polytypism additionally allows us to engineer the physical properties, *e.g.*, band structure, while valence and conduction bands vary for different polytypes.[6,33] In a previous work we reported on the effect of polytypism on the physical properties (*i.e.*, thermal and electrical conductivity and Seebeck coefficient) of ternary Cu_2GeSe_3 (CGSe) nanocrystals, which dramatically enhanced their thermoelectric figure of merit.[34]

The asymmetric growth of nanocrystals, as well as their size, can be highly correlated with the polarity of the growth direction and the external facets. Polarity is the relative charge residing on the two sites of the dumbbell units, which comprise a pair of atoms, a cation on one side and an anion on the other side.[35] In tetrahedrally coordinated semiconductors, polarity determines the internal electric field of the crystal. Recently it has been shown that in semiconductors the growth direction of one-dimensional nanostructures such as nanowires[28] and in general nonplanar structures such as tripods and tetrapods is driven by polarity.[29] Polarity also has a remarkable influence on physical properties of the compounds,[36−38] for instance, the emission wavelength in light emitting and laser diodes.[39,40]

Branching, polytypism, and polarity have been widely studied in II−VI and III−V binary semiconductors, but not in complex Cu-based compounds. Ternary and quaternary materials present a wider variety of tunable parameters and, thus, properties and functionalities associated with the richer composition variability and atomic organization.[41] In this context, as reported by Yang *et al.*,[42] the band structure and energy gap in $Cu_2Ge(S_{1-x}Se_x)_4$ (CGSSe) nanocrystals depend on the chemical composition, as stoichiometry variations cause distortion in the structure. Fan *et al.*[43] also showed that the band gap is tunable by composition changes in $Cu_2ZnSn(S_{1-x}Se_x)_4$ (CZTSSe). However, Liu *et al.*[44] reported that Cu-doping in CCTSe does not cause a significant change in the band structure. The CCTSe band gap is reported experimentally as 0.96 eV[45] and theoretically as 0.98 eV.[44] Nevertheless, no band gap energy has been yet reported on hexagonal $Cu_2Cd_7SnSe_{10}$.

Finally, another important parameter affecting the electronic properties and the band structure in complex materials is the ordering of the cations. As an example, in ordered CCTSe structures, with Cu, Cd, and Sn atoms occupying the cation sites as a stannite structure,[46] conducting and insulating units can be found within the unit cell.[44] Such an ordered p-type semiconductor, with high hole mobilities and Seebeck coefficients, has a high thermoelectric figure of merit. However, random distribution of the cation eliminates this effect and additionally decreases the thermal conductivity, which can further improve the thermoelectric properties. In contrast, it is well known that in chalcopyrite $Cu(InGa)Se_2$ (CIGS) solar cells the presence of CuAu-ordered phases highly deteriorates the device performance, due to the elimination of large quantities of point defects contributing to the CIGS p-type electrical conductivity.[47] It is therefore crucial to determine whether cation ordering (*e.g.*, stannite and kesterite) or random cation distribution in the crystal structures is present in the nanocrystals. This is in fact a quite challenging task, as the differences in the cell parameters of these structures are so tiny that they cannot be distinguished by conventional X-ray and electron diffraction methods.

In the present work we study the influence of polytypism and polarity on the branching mechanism in the Cu-based quaternary semiconductor CCTSe. We show how these issues control the morphology of the nanocrystals and modulate their properties. We present theoretical studies *via ab initio* simulations revealing the impact of these phenomena on the electronic properties of CCTSe nanocrystals. Furthermore, by taking advantage of high-angle annular dark-field scanning transmission electron microscopy (HAADF-STEM) imaging for polarity determination, we discuss the pivotal role of the polarity in morphology and growth mechanism of the branched nanocrystals. Finally, the presence/absence of cation ordering in our complex systems will be correlated with the *ab initio* simulations, allowing us to understand the final electronic band structure configuration of the branched CCTSe nanocrystals.

RESULTS AND DISCUSSION

The formation of the CCTSe branched nanocrystals follows a rather complicated mechanism that is different from the formerly reported ones.[8,48,49] The nanocrystal growth, as shown in Figure 1, initiates with nucleation of quasi-spherical Cu_xSe nanoparticles, and after arriving at a critical size, together with gradual diffusion of Sn and Cd, they find tetrahedral facets. Then, on each facet of the tetrahedral nanocrystal another tetrahedron forms, and the morphology changes from a simple tetrahedron to a *pentatetrahedron*.[50] Afterward, the secondary tetrahedra branch out from the top, and therefore, depending on the number of branches from 1 to 4, monopods, bipods, tripods, or tetrapods form, respectively. Figure 2 shows high-resolution TEM (HRTEM) images of all these structures, associated with 3D atomic models in order to clearly understand their morphology. This growth mechanism is also presented in the TEM images of Figure SI 1 (see Supporting Information) by observing the nanocrystals in different reaction times.

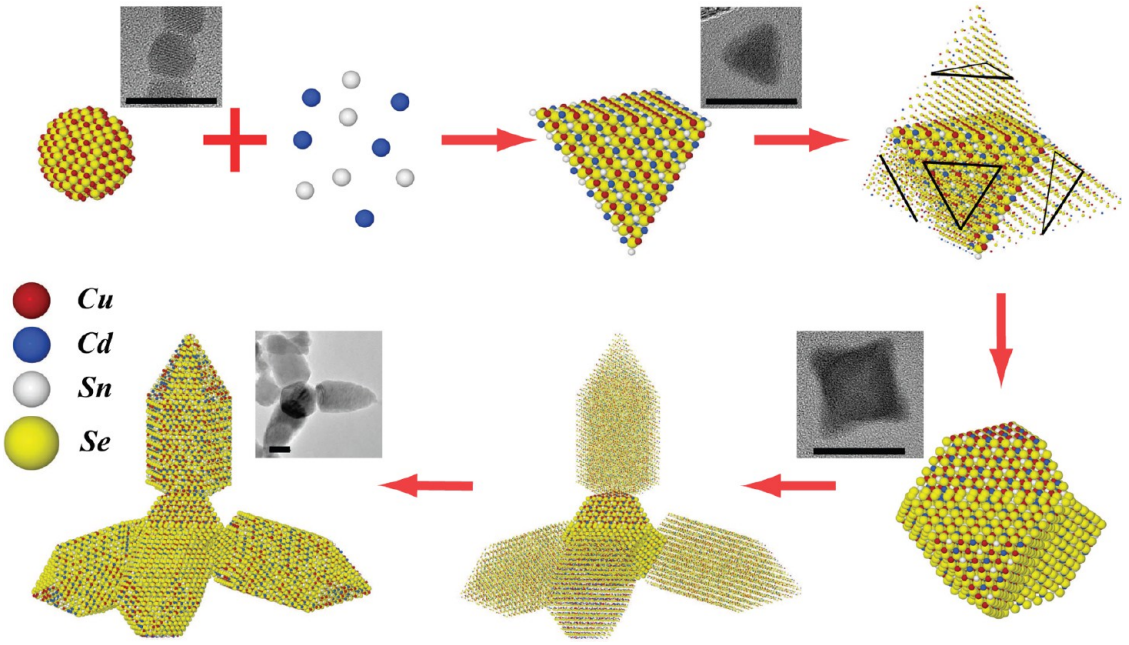

Figure 1. Scheme of CCTSe tetrapod growth from a Cu_xSe quasi-spherical seed, which after diffusion of Cd and Sn finds tetrahedral faceting; then the secondary tetrahedra grow on the initial seed, resulting in the formation of a pentatetrahedron, which after branching changes to a tetrapod. TEM images are displayed for each synthesis step. Scale bars are 20 nm.

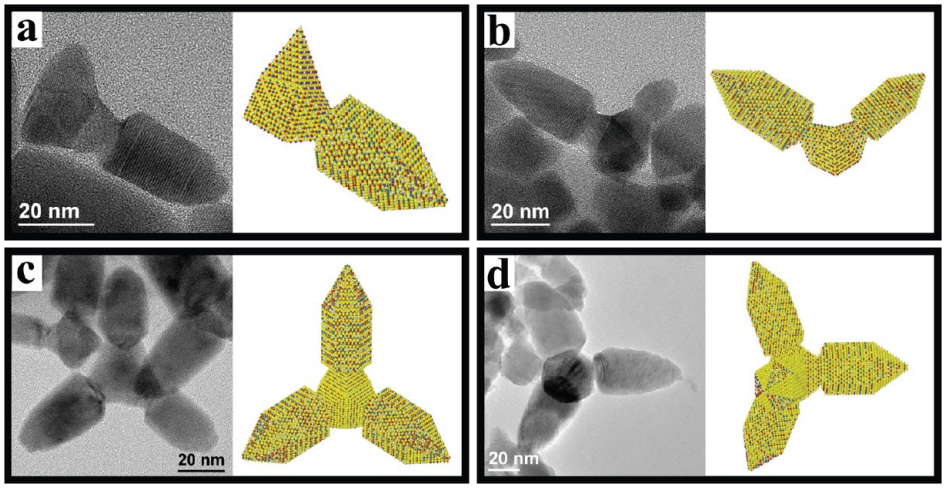

Figure 2. TEM micrographs of different polypods: (a) monopod, (b) bipod, (c) tripod, and (d) tetrapod CCTSe nanocrystals associated with 3D atomic models.

The size of the Cu_xSe nanocrystals is determined by the concentration of amine in solution; that is, the larger the amine concentration, the smaller the size of the obtained nanocrystals. The size of the initial Cu_xSe nanocrystals determines the final size of the tetrahedral and pentatetrahedral nanocrystals. In Figure SI 2 TEM micrographs and size histograms of the nanocrystals obtained by using different concentrations of hexadecylamine (from 1 to 7 mM) are presented (see Supporting Information).

The newly synthesized CCTSe polypod structures are the result of the polytypic branching of the pentatetrahedral nanocrystals (acting here as seeds).[46] The tetrahedral CCTSe nanocrystals have four facets of {112} planes. These nanocrystals have a tetragonal crystal structure (space group $I\bar{4}2m$) with c parameter almost twice that of a and b. Essentially, the unit cell is almost the same as a cubic zinc-blende cell like sphalerite ZnS, where the ordering of the cations as a stannite structure makes it tetragonal. Zinc-blende, a cubic diamond-like structure in the $F\bar{4}3m$ space group, is the main polytype in many different tetrahedrally coordinated semiconductors. Thus, (112) planes of this structure are equivalent to (111) planes of zinc-blende with the highest packing density, which can explain the minimum surface energy of (112) faceting.

There are eight different {112} planes; four of them are cation terminated (cation-polar) and the other four are anion terminated (anion-polar). As a matter of fact,

polarity is the reason that the seed forms as a tetrahedron with four {112} facets, although there are eight possible {112} facets. The cation-polar surfaces in CCTSe appear to be preferred during the growth in solution, and thus the seed forms as a tetrahedron. Octahedral seeds indicating equal growth along cation- and anion-terminated planes were not observed. We will further verify the cation-polarity, which was mainly observed in the case of compounds such as ZnO.[36] In contrary, most other semiconductor binary systems are anion-polarized when grown as nonplanar nanostructures.[29,36,51,52]

At the critical tetrahedron size, a twin occurs on each of the four cation-polar {112} facets of the initial tetrahedra. Twinning consists of a 180° rotation of the structure along the {112} axis, and hence, the growth continues by formation of secondary tetrahedra on top of every triangular {112} facet of the initial and leads to the emergence of pentatetrahedral morphology. Therefore, the nanocrystal morphology changes from tetrahedral to pentatetrahedral, with 12 free facets, all from the {112} plane family and anion-polar. In fact, the occurrence of this twin boundary that confines the size of the CCTSe pentatetrahedral nanocrystal is correlated to the size of the initial Cu_xSe seeds and hence the amine concentration.

The excess of Cd in the solution and the presence of phosphonic acids lead to the formation of polypod structures from the pentatetrahedral nanocrystals. A video in ref 53 schematically shows the growth steps and the 3D morphology of a CCTSe tetrapod. The formation of branches in tripods and tetrapods is usually accompanied by the change in the crystal structure. Most of the known polypod branches are composed of hexagonal wurtzite structure or, equivalently, a highly twinned polytype.[54] In this material, interestingly, the structural change from zinc-blende to wurtzite is associated with chemical composition changes, as the only stable CCTSe compound with hexagonal symmetry reported in the literature is $Cu_2Cd_7SnSe_{10}$ (space group $P6_3mc$).[55] Details of the chemical composition analysis can be found in the Supporting Information. Figure SI 3 shows an annular dark-field (ADF)-STEM image associated with EELS compositional maps. The seed has the stoichiometry of $Cu_2CdSnSe_4$ structure, but the content of Cd in the branch is considerably higher, matching $Cu_2Cd_7SnSe_{10}$ stoichiometry. The results of EELS analysis are in agreement with those of HRTEM, as shown in Figure 3.

The cell parameters of this structure are slightly different from the predicted wurtzite. Following the common rules of wurtzite/zinc-blende polytypism, $a_{WZ} = (0.70 \pm 0.03) \times a_{ZB}$ and $c_{WZ} = (0.87 \pm 0.03) \times a_{ZB}$, we expected to have a hexagonal structure with $a = b \simeq 4.0$ Å and $c \simeq 6.6$ Å roughly; however, the experimentally obtained structure, matching the one of ref 55, is slightly bigger: $a = b \simeq 4.30$ Å and $c \simeq 7.03$ Å. These experimental values are fully consistent with the prediction of *ab initio* calculations. Four different wurtzite structures with different random distributions of Cu, Cd, and Sn were simulated (see Figures SI 5 and SI 6 in the Supporting Information). All four structures lead to similar relaxed lattice parameters, independently of the specific atomic arrangement, with mean values of (standard deviation in parentheses) $a = 4.305(0.004)$ Å, $b = 4.35(0.02)$ Å, and $c = 7.09(0.03)$ Å. This result is in good agreement with the experimental determinations and suggests that the expansion in the cell parameter can be merely attributed to the higher concentration of Cd, which is a heavier element than Cu.

Figure 3 shows HRTEM images of a CCTSe bipod. Due to the 3D structure of tripods and tetrapods, it is quite unlikely to have them in an appropriate zone axis for HRTEM analysis while they lie on TEM carbon/graphene grids. Therefore, for all the studies of this report we choose monopods and bipods which have 2D structures that give all crucial crystallographic information we require. The result can then be correlated to tripod and tetrapod morphologies.

In the HRTEM image of Figure 3a and d, the twin defect at the border of the initial tetrahedral seed and the tetrahedral extensions are indicated. Both initial and extended tetrahedra have tetragonal structure. In the corresponding fast Fourier transform (FFT) power spectra in Figure 3c one can see how the structure is mirrored along $(\bar{1}12)$ and $(11\bar{2})$ planes in the left and the right extensions, respectively. Dot lines show the twin boundaries, and dashed lines correspond to the $(11\bar{2})$ and $(\bar{1}12)$ planes. These lines also show the dumbbell units in each atomic plane, which find a different arrangement when it arrives at the wurtzite structure of the branches. The zigzag form of the red lines corresponds to a dumbbell orientation in wurtzite flipping from one atomic layer to the other. This can be seen in the atomic models in Figure 3b, where the dumbbell orientation is indicated by white arrows on the side view of wurtzite and zinc-blende-like (ZB′) structures.

In Figure 3a different regions are numbered to which the power spectra of Figure 3c correspond. Region I is the initial tetrahedral seed with tetragonal structure. Regions II and III are two of the secondary tetrahedra that form the pentatetrahedral nanocrystals. Regions IV and V are the branches with wurtzite structure as observed in the corresponding power spectra. The lower-center power spectrum in Figure 3c is indeed taken from regions I, II, and III, all together showing the reflections of the different regions in different colors. This power spectrum reveals how the reflections are mirrored along the dashed lines. The blue and green dashed lines indicate the direction of twinning (perpendicular to the twin planes) in the left and right tetrahedra, respectively. Multiplicity of twin boundaries gives rise to the occurrence of wurtzite branches.

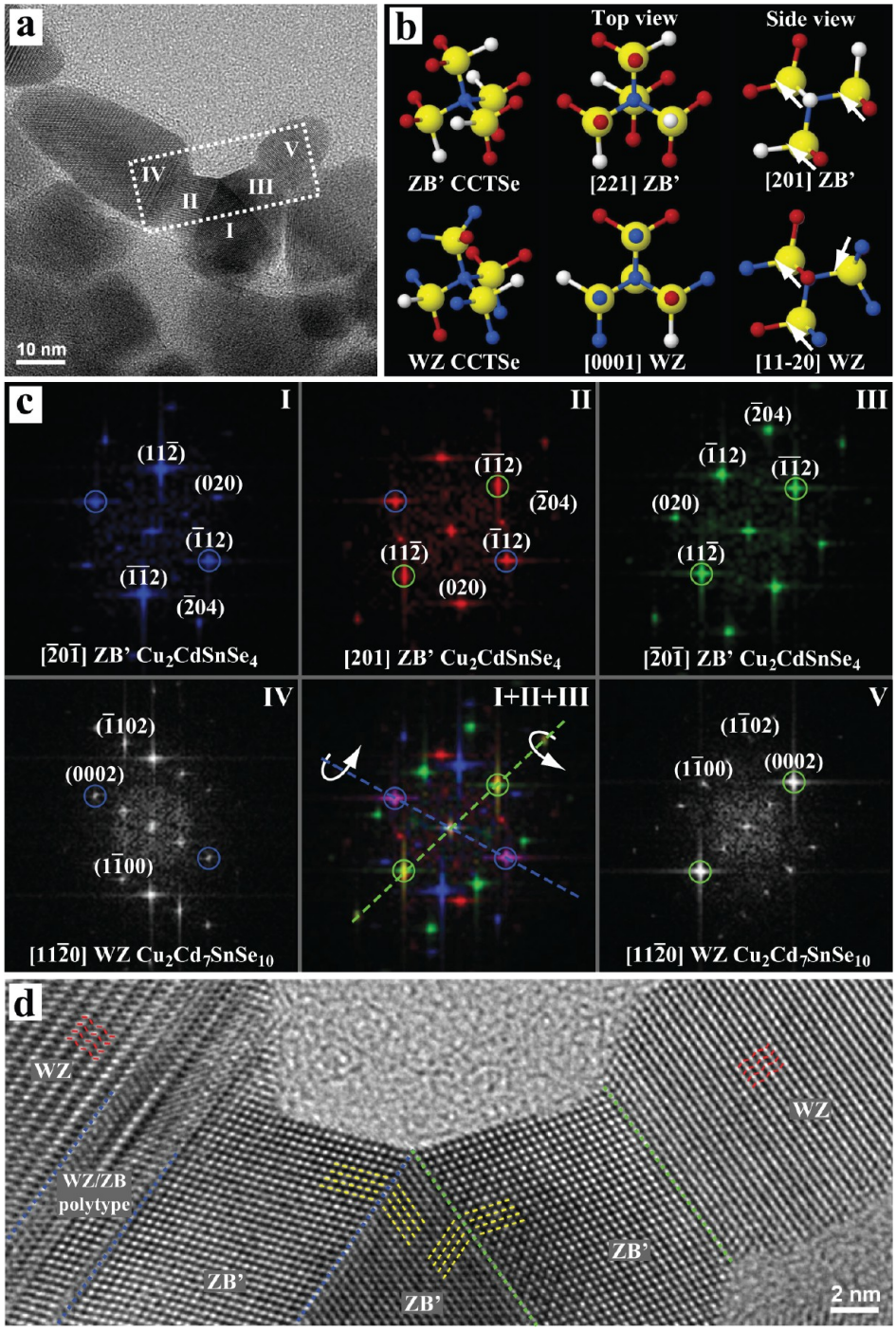

Figure 3. HRTEM analysis on a bipod. (a) TEM micrograph showing the whole bipod and indicating the zones with Greek numbers: (I) the ZB-like initial tetrahedron, (II, III) the secondary ZB-like tetrahedra, and (IV, V) the WZ branches. (b) Atomic models showing the structural difference between ZB-like and WZ. (c) Power spectra corresponding to each zone from I to V. (d) HRTEM micrograph showing the atomic planes and twinning in the bipod.

At the beginning of the left branch a kind of polytype between zinc-blende and wurtzite takes place as the number of twins is not yet sufficient to reach wurtzite structure.

It is evidenced that the faceting of the seed and the growth direction of branches in the tetrapods are cation-polar. Interestingly, the polarity of the surface facets changes from tetrahedron to pentatetrahedron. The external facets of the tetrahedra are cation-polar, while those of the pentatetrahedra are anion-polar. Lateral surfaces of the branches are nonpolar ({11$\bar{2}$0} facets); nonetheless, the start of branching comes from a plane that has the same polarity as initial tetrahedra and inverse polarity with respect to the external facets of the pentatetrahedra. This is schematically shown in Figure 4. Cation- and anion-polarity are shown by

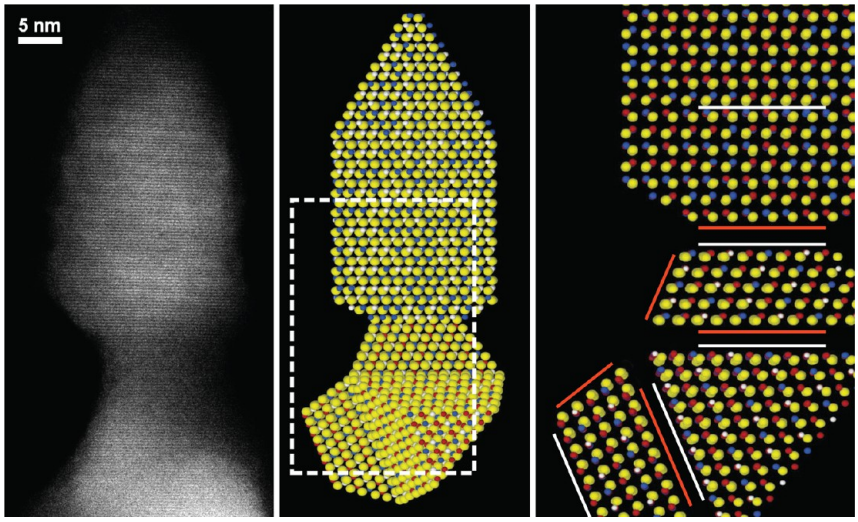

Figure 4. Polarity in a monopod: the first tetrahedral seed grows with cation polarity (indicated by white lines), the secondary tetrahedra grow with the same polarity, but with anion-polar lateral surfaces (indicated by red lines). The top facet with cation-polarity is ready for branching. Branches also keep cation-polarity. Lateral surfaces of the wurtzite branches are nonpolar.

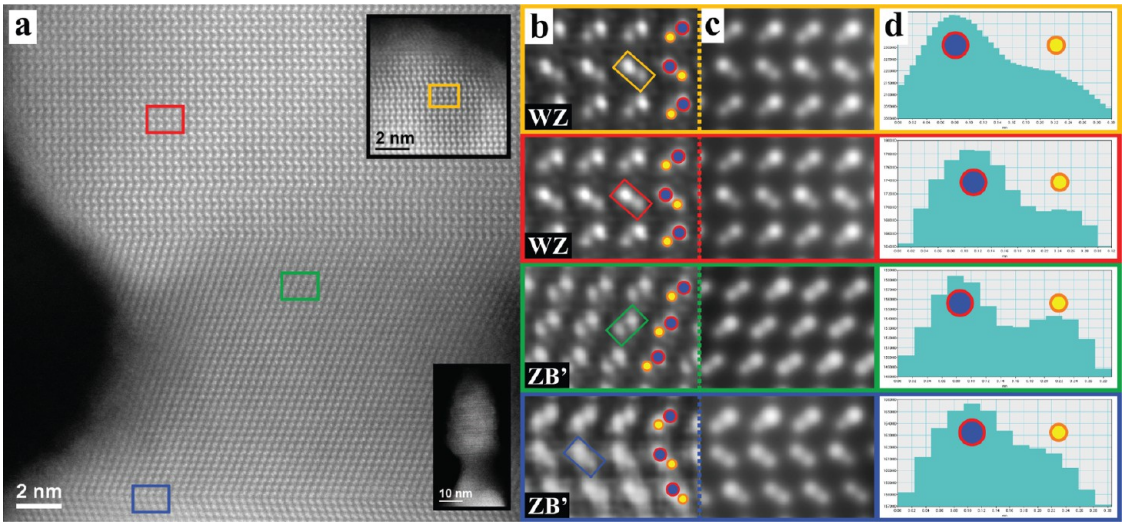

Figure 5. Polarity: (a) HAADF-STEM from $[201]_{ZB'}/[11\bar{2}0]_{WZ}$ zone axis, (b) the magnified zones indicated on image (a) by colored rectangles after deconvolution of the STEM probe, (c) linear simulations of the STEM images (b), and (d) the intensity profile on one dumbbell unit (indicated on images (b)) in (yellow) the top part of the branch, (red) the beginning of the branch, (green) the secondary tetrahedron, and (blue) the border of the initial and the secondary tetrahedra.

white and red lines, respectively. Taking into consideration that polarity inversion is not energetically favorable,[28,29,36] only an anion-polar surface tetrahedron can grow on a cation-polar-surfaced seed in order to form the pentatetrahedral morphology (cation-polar facets are {112}, $\{\bar{1}\bar{1}2\}$, $\{1\bar{1}2\}$, and $\{\bar{1}12\}$, while anion-polar facets are $\{1\bar{1}2\}$, $\{\bar{1}12\}$, $\{11\bar{2}\}$, and $\{\bar{1}\bar{1}2\}$; for example, a secondary tetrahedron accommodates on the {112} facet of the initial seed with $\{\bar{1}\bar{1}2\}$ facet, and the other three anion-polar facets are free). Cation-polarity is kept along the growth direction; however, due to the twin boundary, lateral facets change from cation-polar to anion-polar ones, and this can be an adequate explanation for growth confinement with these new facets (see Figure 5). The {112} anion-polar facets are confined to their joining point, which forms the peak of the tetrahedron (note that in practice the secondary tetrahedra do not have such sharp peaks, and the corners are rounded, ending with the cation-polar facet of the initial tetrahedron on which they were grown; see Figure 1). Therefore, the nanocrystals have no possibility to grow further if they only follow this mechanism. However, the branching mechanism plays a key role in allowing the nanocrystals to grow more. Here, nevertheless, from the assistance of the twinning mechanism the structure switches from tetrahedral (zinc-blende-like) to wurtzite. Prismatic wurtzite branches comprise six nonpolar lateral facets and a cation-polar growth direction that theoretically has no limit for growth. It seems that nonpolar surfaces have

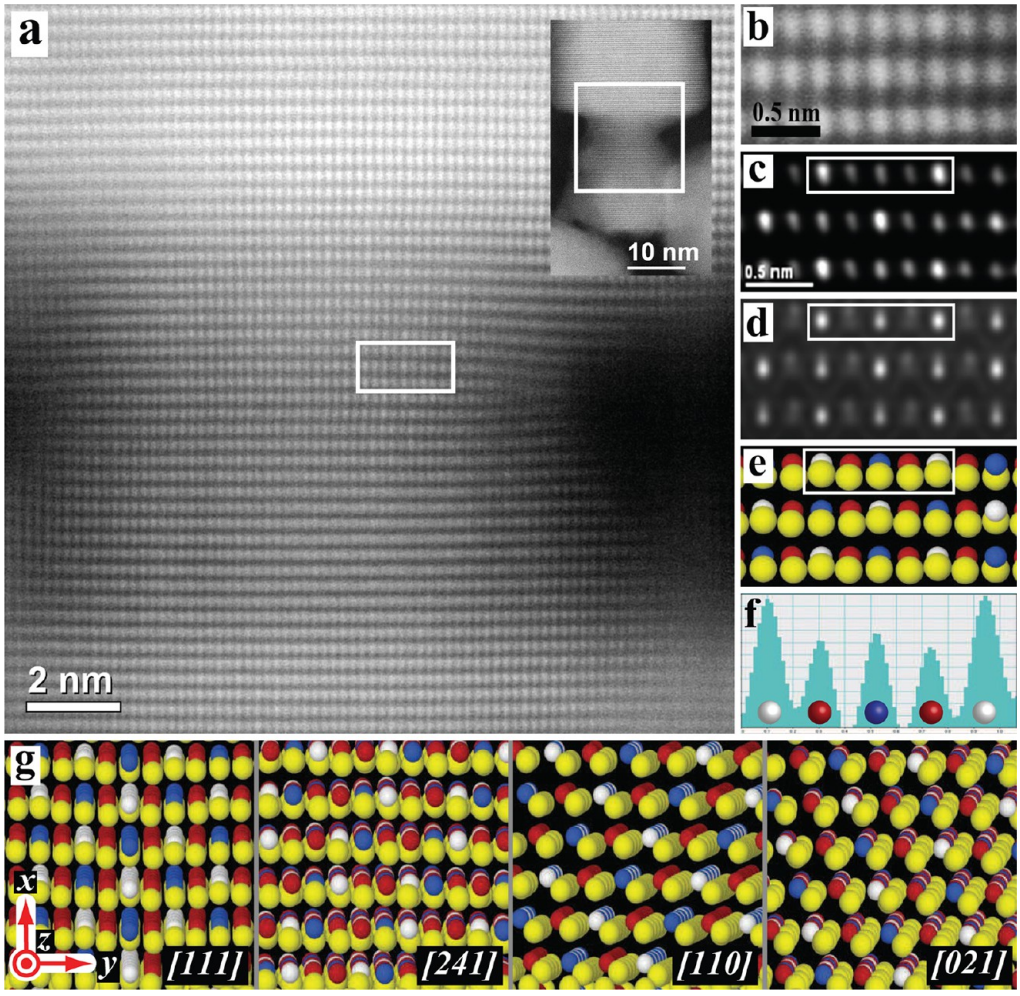

Figure 6. (a) Atomic-resolution HAADF-STEM image from the $[111]_{ZB}$ zone axis of the CCTSe tetragon (ZB′), (b) a deconvolved and magnified part of image (a), (c) filtered and (d) simulated (linear simulation), in order to clearly show the ordering effect, which is correlated with (e) the 3D atomic model. (f) Intensity profile taken from image (c). (g) 3D atomic models of a secondary ZB-like tetrahedron from four different zone axes showing why the ordering effect can only be seen from the $[111]_{ZB'}$ zone axis. Note that the models are posed slightly off from the zone axis, in order to facilitate visualization of the cation atomic columns.

the freedom to grow further, but not as fast as the cation-polar one. Thus, while the branches grow longer, they also thicken laterally with a slower rate along the nonpolar facets. Nevertheless, during this process, the secondary tetrahedra with anion-polar facets maintain their size and create a neck-like zone, because growth in anion-polar facets is confined.

In Figure 5 polarity is determined on the HAADF-STEM micrograph in different regions of a monopod from the $[201]_{ZB'}/[11\bar{2}0]_{WZ}$ zone axis ($[201]_{ZB'}$ in our ordered tetragonal structure is the same as $[101]_{ZB}$ in cubic zinc-blende). Magnified and shown on the right are the twinned interface between the initial and the secondary tetrahedra in blue, secondary tetrahedron in green, start of the branch in red, and the tip of the branch in yellow. In the high-resolution STEM image of Figure 5a, the bottom inset shows the whole monopod, and the top inset shows the polarity in the tip. The zones indicated by colored rectangles are deconvolved and magnified in Figure 5b in order to see the polarity clearly. In this part the experimental image is numerically elaborated in order to remove the effect of the STEM probe. Toward this aim we applied the iterative maximum entropy deconvolution algorithm described in ref 56. Moreover, these STEM images are simulated and shown in Figure 5c in order to confirm the experimental results with theory. The simulated STEM images of the entire monopod are revealed in Figure SI 4 (see Supporting Information). The corresponding intensity profiles are revealed in Figure 5d.

We point out that the polarity determination in the seed is more difficult than in the branch. The intensity difference between the anion and the cation is less in the zinc-blende-like seed, which is due to the stoichiometry of the structure. The intensity in STEM increases monotonically with the atomic number (Z) of the elements in each point. In the case of the seeds the difference between the average Z of the anion and the average of cations is rather small. However, still the polarity is distinguishable from the intensity profiles.

As a matter of fact, in the literature, even smaller differences in compounds such as GaAs were utilized for polarity determination.[28,36] In the branch the Cd content is much higher ($Cu_2Cd_7SnSe_{10}$ stoichiometry), and consequently, as Cd is much heavier than Se, polarity determination is quite straightforward. Details of the relation between the intensity and the atomic number in cation sites are described in the Supporting Information.

Another important difference between the structure of the seed and the branch is the ordering of the cations. It is observed that in the seed the cations, Cu, Cd, and Sn, keep the stannite ordering, while in the branches they are randomly distributed in the cation sites. The HAADF micrograph of Figure 6a reveals the ordering of the cations in the seed. Essentially, the $[201]_{ZB'}$ zone axis, which is best for visualization of the dumbbell units, does not allow us to see the cation ordering. This is because in each cation column in projection, Cu, Cd, and Sn atoms overlap. To facilitate comprehension, a 3D atomic model of this structure is shown from different angles in Figure 6f. As a convention, we define the viewing coordination as *x*, horizontal; *y*, vertical; and *z*, viewing axis normal to the drawing plane. The three proper zone axes for polarity measurements are not suitable for cation-ordering visualization, because the atomic Cu, Cd, and Sn columns superpose. In contrast, the [111] viewing direction is the only one that allows observing the stannite ordering since none of these elements are superposed with each other (see Supporting Information). It can be seen in Figure 6f that from this zone axis, in the *x* direction, vertical Cu columns and Cd−Sn columns alternate and, further, Cd columns and Sn columns alternate in the *y* direction. Note that in this figure the models are posed slightly off from the zone axis, in order to facilitate the visualization of the cation atomic columns.

Figure 6a displays an HAADF-STEM image of the narrowest part of the seed (indicated in the inset) of a monopod where the structure is still zinc-blende-like. For better visualization one part is magnified and deconvolved (Figure 6b) and frequency-filtered (Figure 6c). Also, linear STEM image simulation is revealed (Figure 6d). In the intensity profile in Figure 6f, taken from the filtered image (Figure 6c), one can determine the position of cations with Sn−Cu−Cd−Cu−Sn stannite ordering. The good agreement between the experimental images (Figure 6a and b) and the calculated image (Figure 6d) from the stannite atomic model (Figure 6e) confirms the presence of ordering. Note that the intensity of the Cd columns is closer to that of the Cu columns than Sn columns, *i.e.*, less than what is expected in stannite structure. This is attributed to Cu-doping in the seed, as also confirmed by EELS maps. From the EELS maps of Figure SI 3 we inferred that the content of Cd in the seed is low; thus the stoichiometry is $Cu_{2+x}Cd_{1-x}SnSe_4$.

By atomic resolution HAADF-STEM we have shown that the zinc-blende-like seeds show consistence in

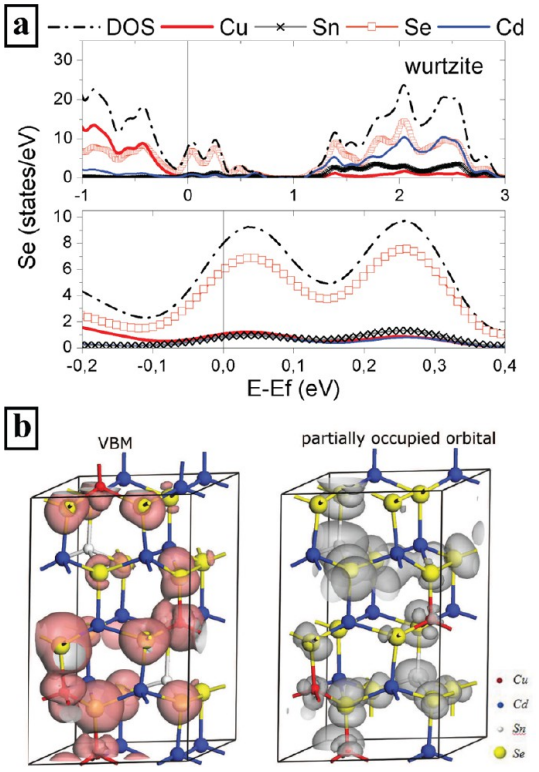

Figure 7. (a) Projected density of electron state (PDOS) of the WZ structure. There is a continuum of states around the Fermi level (E_F = 0 eV). (b) (left) The highest occupied energy state (valence band maximum, VBM) is mainly associated with Cu−Se centers, and (right) the first partially occupied state is localized on Se−Sn and Se−Cu bonds.

ordering, whereas the wurtzite branches consist of a disordered compound with random distribution of Cu, Cd, and Sn in cation sites, and the Cd content is by far higher than in the pentatetrahedral seeds. The $[Cu_2Se_4]$ and $[CdSnSe_4]$ tetrahedral slabs, of which the zinc-blende-like stannite CCTSe structure is comprised, are considered as electrically conducting and electrically insulating units, respectively.[44] In a previous work on this material we found experimental evidence for significant changes in electrical and thermal resistance of the compound caused by lattice distortion as a result of Cu-doping. Consequently, Cu-doping showed significant influence on the electrical and thermal resistance of the compound and thus its thermoelectric figure of merit.[46] The experimental results were in good agreement with *ab initio* simulations of the electronic band structure. Here also we calculated the valence band maximum (VBM) and conduction band minimum (CBM) of distorted wurtzite structure in order to compare the electronic band structure of this compound with that of the zinc-blende-like ordered stannite CCTSe. For the case of random cation distribution, various 2 × 2 × 2 cells were created keeping the stoichiometry, in order to ensure that the specific local distributions do not affect the final results (see Figure SI 5 and the calculation details in the Supporting Information).

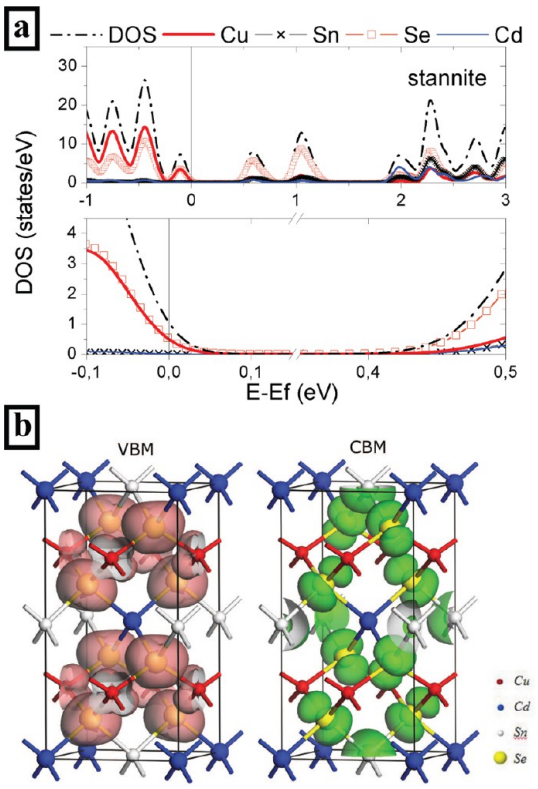

Figure 8. (a) Projected density of electron states (PDOS) of the stannite (ZB-like) structure, which exhibits a clear band gap. (b) (left) Again, the highest occupied energy state (valence band maximum, VBM) is mainly associated with Cu−Se centers, but (right) the lowest unoccupied energy state (conduction band minimum, CBM) is localized only on Se−Sn bonds.

These simulations revealed that Fermi energy lies within a band in the case of the distorted wurtzite CCTSe. Thus, this compound has a quasi-metallic character (see Figure 7), in contrast with the semiconducting character of the stannite structure, with a density functional theory (DFT) band gap of 0.5 eV (Figure 8).[57] While in stannite the VBM is localized in Cu−Se dimers and the CBM is around Sn−Se, the partially filled band of the distorted wurtzite structure is due to a combination of both Sn−Se and Cu−Se localized orbitals. As can be seen in Figures 7 and 8, the spatial distribution of these transport active orbitals is strongly influenced by the specific atomic arrangement: in the stannite structure, there are orbitals regularly arranged and localized in specific planes, creating discontinuities in the transport paths, whereas they follow the specific atomic random distribution in the distorted wurtzite, leading to more tortuous but more highly connected transport paths.

Accordingly, CCTSe branched nanocrystals have a narrow-band-gap seed and metallic pods. Such nanometric heterostructures with metallic branches can be used as perfect epitaxial Schottky contacts. On the other hand, the seed with the semiconducting nature can be used for several applications such as thermoelectrics, photovoltaics, and sensing. Moreover, such morphology-modulated polypods with metallic branches may have enhanced plasmonic applications, as copper vacancies in such materials give rise to composition-dependent localized surface plasmon resonance (LSPR).[20,58−64]

CONCLUSION

In summary, we report on the control of polytypic branching in complex quaternary chalcogenide (CCTSe) nanocrystals driven by polarity. Their chemical and crystallographic structure changes from the seed to the branches and leads to dramatic changes in the physical properties. The initial seeds with zinc-blende-like stannite structure have pentatetrahedral morphology and branch out, giving rise to formation of polytypic polypods with wurtzite legs while keeping the cation polarity until the end. The simulation of the electronic band structures shows that as a result of polytypism, the chemical composition change, and lack of cation ordering in the pods, the energy band gap shrinks, the Fermi energy shifts into the conduction band, and the branches change from semiconducting to quasi-metallic character. Such an interesting combination forms a 100% epitaxial interface between the metallic pods and the semiconducting seeds, which can be used for novel applications such as surface plasmonic devices and Schottky barriers between the metallic pods and the semiconducting seeds. Polarity and ordering determination was possible only by dint of the novel microscopy techniques, *i.e.*, aberration-corrected STEM imaging and spectroscopy, corroborated by STEM image simulations. This work indeed proves the potential of growth nanoengineering by controlling the branching, polytypism, polarity, and cation ordering and how it may influence the final physical properties of nanomaterials. The present polarity-induced polypod growth mechanism can be generalized to the rest of Cu-based chalcogenide nanostructured materials.

METHODS

Colloidal CCTSe nanocrystals were prepared following a one-pot procedure similar to the one previously reported.[46] Copper(I) chloride (50 mg, 0.5 mmol), cadmium oxide (33 mg, 0.25 mmol), tin(IV) chloride pentahydrate (88 mg, 0.25 mmol), hexadecylamine (1230 mg, 5 mM), and *n*-octadecylphosphonic acid (33 mg, 0.1 mmol) were dissolved in 10 mL of 1-octadecene (ODE). The solution was heated under argon flow to 200 °C and maintained at this temperature for 1 h to remove water and other low-boiling-point impurities. Afterward, the mixture was heated to the reaction temperature (285 °C). The selenium solution was prepared by dissolving selenium(IV) oxide in ODE under an argon atmosphere at 180 °C. The selenium

solution (4 mL, 3 mM) was rapidly injected through a septum into the reaction flask. Following the injection, the temperature dropped to around 260 °C and then slowly recovered to 285 °C. The solution was kept at a temperature between 260 and 285 °C for 1 to 5 min and then quickly cooled. The formation of CCTSe could be qualitatively followed by the color change of the mixture from an initial light yellow to green and eventually black color of the solution containing the CCTSe nanocrystals. Tetrahedra were obtained with a reaction time of 1 min. Longer reaction times, 5 min, yielded pentatetrahedra. During the cooling of the mixture, 3 mL of oleic acid was added at ~70 °C to replace the weakly bonded HDA. The crude solution was mixed with 10 mL of chloroform and sonicated at 50 °C for 5 min. The CCTSe nanocrystals were isolated by centrifugation at 4000 rpm during 5 min and purified by multiple precipitation/redispersion steps. Branched polytypic nanocrystals were prepare very much as described above with excess Cd in the solution and in the presence of phosphonic acids.

The crystal structure, morphology, and faceting of the nanocrystals were investigated by high-resolution transmission electron microscopy (HRTEM) and atomic resolution aberration-corrected high-angle annular dark-field (HAADF) scanning transmission electron microscopy (STEM) imaging. HRTEM was performed in a Jeol 2010F microscope, equipped with a field emission gun and operated at 200 keV. HAADF-STEM was performed on a FEI Titan 60-300 Ultimate microscope ("PICO") operated at 200 keV, equipped with a high-brightness electron gun, a C_s probe corrector, and a Gatan Quantum postcolumn energy filter system.

For polarity determination there are a few methods previously developed, such as homoepitaxy, convergent beam electron diffraction, or scanning tunneling microscopy, which besides being inconvenience do not have enough spatial resolution to determine the polarity at the atomic scale or changes in polarity if there are any. In contrast, aberration-corrected transmission electron microscopes offer the possibility of direct polarity measurement, as they can reach sub-angstrom resolutions. By means of atomic-resolution STEM techniques such HAADF[37] or the recently developed annular bright-field (ABF) STEM,[65−67] we can even visualize light atoms (*e.g.*, H, N, and O) within the dumbbells,[30,36,51,68] find single atoms in dissimilar atomic columns (*e.g.*, a single Au atom within GaAs nanowires),[69] or distinguish between two atoms with close atomic numbers (*e.g.*, Ga and As).[29,36] In this work we take advantage of HAADF-STEM imaging, where, due to the comparatively small difference between the average atomic number of the cations (Cu, Cd, Sn) and the anion (Se), polarity determination is rather challenging.

In addition, three-dimensional atomic simulation was performed using the Rhodius software package,[70] which allows creating complex atomic models.[29,50] The STEM_CELL software tool[56,71] was utilized for linear STEM image simulations in order to corroborate the experiment with theoretical work.

For the *ab initio* calculations SIESTA code[72,73] was used, which combines DFT with norm-conserving Troullier−Martins[74] pseudopotentials and local basis set functions. Local density approximation[75,76] for the exchange−correlation functional was used. All the calculations were performed with a cutoff of 250 Ry on the electron density, standard double-ζ basis sets for all the atoms, and a Monkhorst−Pack grid of $3 \times 3 \times 2$ for the wurtzite structure and $4 \times 4 \times 2$ for the stannite structure. Positions and cell parameters were relaxed until atomic forces were less than 0.05 eV/Å.

Conflict of Interest: The authors declare no competing financial interest.

Acknowledgment. The research leading to these results has received funding from the European Union Seventh Framework Programme under grant agreement 312483-ESTEEM2 (Integrated Infrastructure Initiative I3) for using advance electron microscopes at ER-C Jülich. J.A. acknowledges the funding from the Spanish MICINN project MAT2010-15138 (COPEON) and Generalitat de Catalunya 2009 SGR 770. R.R.Z. acknowledges the former. The authors would also like to thank the TEM facilities in Serveis Cientificotecnics from Universitat de Barcelona. N.G.-C. acknowledges the Spanish MECD for her Ph. D. grant in the FPU program. JR and RZ acknowledge funding from MULTICAT and NANOENESTO projects.

Supporting Information Available: Further results and explanations are provided in five sections: (i) Growth mechanism and synthesis conditions, (ii) EELS compositional maps, (iii) Intensity of cation and anion atomic columns in HAADF images, (iv) Proper zone axes for dumbbell and ordering visualization, (v) Electronic band structure, *ab initio* calculations. This material is available free of charge *via* the Internet at http://pubs.acs.org.

REFERENCES AND NOTES

1. Aldakov, D.; Lefranois, A.; Reis, P. Ternary and Quaternary Metal Chalcogenide Nanocrystals: Synthesis, Properties and Applications. *J. Mater. Chem. C* **2013**, *1*, 3757–3776.
2. Ibáñez, M.; Zamani, R.; Lalonde, A.; Cadavid, D.; Li, W.; Shavel, A.; Arbiol, J.; Morante, J. R.; Gorsse, S.; Snyder, G. J.; *et al*. $Cu_2ZnGeSe_4$ Nanocrystals: Synthesis and Thermoelectric Properties. *J. Am. Chem. Soc.* **2012**, *134*, 4060–4063.
3. Ibáñez, M.; Cadavid, D.; Anselmi-Tamburini, U.; Zamani, R.; Gorsse, S.; Li, W.; López, A. M.; Morante, J. R.; Arbiol, J.; Cabot, A. Colloidal Synthesis and Thermoelectric Properties of Cu_2SnSe_3 Nanocrystals. *J. Mater. Chem. A* **2013**, *1*, 1421–1426.
4. Li, W.; Ibáñez, M.; Zamani, R. R.; García-Castelló, N.; Gorsse, S.; Cadavid, D.; Prades, J. D.; Arbiol, J.; Cabot, A. $Cu_2HgSnSe_4$ Nanoparticles: Synthesis and Thermoelectric Properties. *CrystEngComm* **2013**, *15*, 8966–8971.
5. Li, H.; Kanaras, A. G.; Manna, L. Colloidal Branched Semiconductor Nanocrystals: State of the Art and Perspectives. *Acc. Chem. Res.* **2013**, *46*, 1387–1396.
6. Li, J.; Wang, L.-W. Shape Effects on Electronic States of Nanocrystals. *J. Mater. Chem. A* **2003**, *3*, 1357–1363.
7. Milliron, D. J.; Hughes, S. M.; Cui, Y.; Manna, L.; Li, J.; Wang, L.-W.; Alivisatos, A. P. Colloidal Nanocrystal Heterostructures with Linear and Branched Topology. *Nature* **2004**, *430*, 190–195.
8. Manna, L.; Milliron, D. J.; Meisel, A.; Scher, E. C.; Alivisatos, A. P. Controlled Growth of Tetrapod-Branched Inorganic Nanocrystals. *Nat. Mater.* **2003**, *2*, 382–385.
9. Fiore, A.; Mastria, R.; Lupo, M. G.; Lanzani, G.; Giannini, C.; Carlino, E.; Morello, G.; De Giorgi, M.; Li, Y.; Cingolani, R.; *et al*. Tetrapod-Shaped Colloidal Nanocrystals of II−VI Semiconductors Prepared by Seeded Growth. *J. Am. Chem. Soc.* **2009**, *131*, 2274–2282.
10. Gur, I.; Fromer, N. A.; Chen, C.-P.; Kanaras, A. P.; Antonios, G. Alivisatos Hybrid Solar Cells with Prescribed Nanoscale Morphologies Based on Hyperbranched Semiconductor Nanocrystals. *Nano Lett.* **2007**, *7*, 409–414.
11. Miszta, K.; de Graaf, J.; Bertoni, G.; Dorfs, D.; Brescia, R.; Marras, S.; Ceseracciu, L.; Cingolani, R.; van Roij, R.; Dijkstra, M.; *et al*. Hierarchical Self-Assembly of Suspended Branched Colloidal Nanocrystals into Superlattice Structures. *Nat. Mater.* **2011**, *10*, 872–876.
12. Choi, C. L.; Koski, K. J.; Sivasankar, S.; Alivisatos, A. P. Strain-Dependent Photoluminescence Behavior of CdSe/CdS Nanocrystals with Spherical. *Nano Lett.* **2009**, *9*, 3544–3549.
13. Ko, S. H.; Lee, D.; Kang, H. W.; Nam, K. H.; Yeo, J. Y.; Hong, S. J.; Grigoropoulos, C. P.; Sung, H. J. Nanoforest of Hydrothermally Grown Hierarchical ZnO Nanowires for a High Efficiency Dye-Sensitized Solar Cell. *Nano Lett.* **2011**, *11*, 666–671.
14. Liu, B.; Zhang, J.; Wang, X.; Chen, G.; Chen, C.; Zhou, D.; Shen, G. Hierarchical Three-Dimensional $ZnCo_2O_4$ Nanowire Arrays/Carbon Cloth Anodes for a Novel Class of High-Performance Flexible Lithium-Ion Batteries. *Nano Lett.* **2012**, *12*, 3005–3011.
15. Cui, Y.; Banin, U.; Björk, M. T.; Alivisatos, A. P. Electrical Transport through a Single Nanoscale Semiconductor Branch Point. *Nano Lett.* **2005**, *5*, 1519–1523.
16. Fu, W.; Qin, S.; Liu, L.; Kim, T.-H.; Hellstrom, S.; Wang, W.; Liang, W.; Bai, X.; Li, A.-P.; Wang, E. Ferroelectric Gated

Electrical Transport in CdS Nanotetrapods. *Nano Lett.* **2011**, *11*, 1913–1918.
17. Jun, Y.-W.; Lee, S.-M.; Kang, N.-J.; Cheon, J. Controlled Synthesis of Multi-armed CdS Nanorod Architectures Using Monosurfactant System. *J. Am. Chem. Soc.* **2001**, *123*, 5150–5151.
18. Morello, G.; Fiore, A.; Mastria, R.; Falqui, A.; Genovese, A.; Creti, A.; Lomascolo, M.; Franchini, I. R.; Manna, L.; Della Sala, F.; *et al*. Temperature and Size Dependence of the Optical Properties of Tetrapod-Shaped Colloidal Nanocrystals Exhibiting Type-II Transitions. *J. Phys. Chem. C* **2011**, *115*, 18094–18104.
19. Utama, M. I. B.; Zhang, Q.; Jia, S.; Li, D.; Wang, J.; Xiong, Q. Epitaxial II–VI Tripod Nanocrystals: A Generalization of van der Waals Epitaxy for Nonplanar Polytypic Nanoarchitectures. *ACS Nano* **2012**, *6*, 2281–2288.
20. Lim, J.; Bae, W. K.; Park, K. U.; zur Borg, L.; Zentel, R.; Lee, S.; Char, K. Controlled Synthesis of CdSe Tetrapods with High Morphological Uniformity by the Persistent Kinetic Growth and the Halide-Mediated Phase Transformation. *Chem. Mater.* **2013**, *25*, 1443–1449.
21. Wang, J.; Singh, A.; Liu, P.; Singh, S.; Coughlan, C.; Guo, Y.; Ryan, K. M. Colloidal Synthesis of Cu_2SnSe_3 Tetrapod Nanocrystals. *J. Am. Chem. Soc.* **2013**, *135*, 7835–7838.
22. López, F. J.; Givan, U.; Connell, J. G.; Lauhon, L. J. Silicon Nanowire Polytypes: Identification by Raman Spectroscopy, Generation Mechanism, and Misfit Strain in Homostructures. *ACS Nano* **2011**, *5*, 8958–8966.
23. Arbiol, J.; Fontcuberta i Morral, A.; Estradé, S.; Peiró, F.; Kalache, B.; Roca i Cabarrocas, P.; Morante, J. R. Influence of the (111) Twinning on the Formation of Diamond Cubic/Diamond Hexagonal Heterostructures in Cu-Catalyzed Si Nanowires. *J. Appl. Phys.* **2008**, *104*, 064312.
24. Conesa-Boj, S.; Zardo, I.; Estradé, S.; Wei, L.; Jean Alet, P.; Roca i Cabarrocas, P.; Morante, J. R.; Peiró, F.; Morral, A. F. i.; Arbiol, J. Defect Formation in Ga-Catalyzed Silicon Nanowires. *Cryst. Growth Des.* **2010**, *10*, 1534–1543.
25. Ek, M.; Borg, B. M.; Johansson, J.; Dick, K. A. Diameter Limitation in Growth of III-Sb-Containing Nanowire Heterostructures. *ACS Nano* **2013**, *7*, 3668–3675.
26. Kriegner, D.; Panse, C.; Mandl, B.; Dick, K. A.; Keplinger, M.; Persson, J. M.; Caroff, P.; Ercolani, D.; Sorba, L.; Bechstedt, F.; *et al*. Unit Cell Structure of Crystal Polytypes in InAs and InSb Nanowires. *Nano Lett.* **2011**, *11*, 1483–1489.
27. Ketterer, B.; Heiss, M.; Uccelli, E.; Arbiol, J.; Fontcuberta i Morral, A. Untangling the Electronic Band Structure of Wurtzite GaAs Nanowires by Resonant Raman Spectroscopy. *ACS Nano* **2011**, *5*, 7585–7592.
28. Uccelli, E.; Arbiol, J.; Magén, C.; Krogstrup, P.; Russo-Averchi, E.; Heiss, M.; Mugny, G.; Morier-Genoud, F.; Nygard, J.; Morante, J. R.; *et al*. Three-Dimensional Multiple-Order Twinning of Self-Catalyzed GaAs Nanowires on Si Substrates. *Nano Lett.* **2011**, *11*, 3827–3832.
29. Utama, M. I. B.; de la Mata, M.; Magén, C.; Arbiol, J.; Xiong, Q. Twinning-, Polytypism-, and Polarity-Induced Morphological Modulation in Nonplanar Nanostructures with van der Waals Epitaxy. *Adv. Func. Mater.* **2013**, *23*, 1636–1646.
30. Utama, M. I. B.; Belarre, F. J.; Magén, C.; Peng, B.; Arbiol, J.; Xiong, Q. Incommensurate van der Waals Epitaxy of Nanowire Arrays: A Case Study with ZnO on Muscovite Mica Substrates. *Nano Lett.* **2012**, *12*, 2146–2152.
31. Utama, M. I. B.; de la Mata, M.; Zhang, Q.; Magen, C.; Arbiol, J.; Xiong, Q. The Growth of Ultralong ZnTe Micro/Nanostructures: The Influence of Polarity and Twin Direction on the Morphogenesis of Nanobelts and Nanosheets. *Cryst. Growth Des.* **2013**, *13*, 2590–2596.
32. Fan, F.-J.; Wu, L.; Gong, M.; Chen, S. Y.; Liu, G. Y.; Yao, H.-B.; Liang, H.-W.; Wang, Y.-X.; Yu, S.-H. Linearly Arranged Polytypic CZTSSe Nanocrystals. *Sci. Rep.* **2012**, *2*, 952.
33. Spirkoska, D.; Arbiol, J.; Gustafsson, A.; Conesa-Boj, S.; Glas, F.; Zardo, I.; Heigoldt, M.; Gass, M. H.; Bleloch, A. L.; Estradé, S.; *et al*. Structural and Optical Properties of High Quality Zinc-Blende/Wurtzite GaAs Nanowire Heterostructures. *Phys. Rev. B* **2009**, *80*, 245325.
34. Ibáñez, M.; Zamani, R.; Li, W.; Cadavid, D.; Gorsse, S.; Katcho, N. A.; Shavel, A.; López, A. M.; Morante, J. R.; Arbiol, J.; *et al*. Crystallographic Control at the Nanoscale To Enhance Functionality: Polytypic Cu_2GeSe_3 Nanoparticles as Thermoelectric Materials. *Chem. Mater.* **2012**, *24*, 4615–4622.
35. Berding, M. A.; Sher, A.; Chen, A. B. Polarity in Semiconductor Compounds. *Phys. Rev. B* **1987**, *36*, 7433–7436.
36. de la Mata, M.; Magén, C.; Gazquez, J.; Utama, M. I. B.; Heiss, M.; Lopatin, S.; Furtmayr, F.; Fernández-Rojas, C. J.; Peng, B.; Morante, J. R.; *et al*. Polarity Assignment in ZnTe, GaAs, ZnO, and GaN-AlN Nanowires from Direct Dumbbell Analysis. *Nano Lett.* **2012**, *12*, 2579–2586.
37. Bertoni, G.; Grillo, V.; Brescia, R.; Ke, X.; Bals, S.; Catellani, A.; Li, H.; Manna, L. Direct Determination of Polarity, Faceting, and Core Location in Colloidal Core/Shell Wurtzite Semiconductor Nanocrystals. *ACS Nano* **2012**, *6*, 6453–6461.
38. Nakamura, S. Current Status of GaN-Based Solid-State Lighting. *MRS Bull.* **2009**, *34*, 101–107.
39. Feezell, D. F.; Schmidt, M. C.; DenBaars, S. P.; Nakamura, S. Development of Nonpolar and Semipolar InGaN/GaN Visible Light-Emitting Diodes. *MRS Bull.* **2009**, *34*, 318–323.
40. Ohta, H.; Okamoto, K. Nonpolar/Semipolar GaN Technology for Violet, Blue, and Green Laser Diodes. *MRS Bull.* **2009**, *34*, 324–327.
41. Pan, J.; Utama, M. I. B.; Zhang, Q.; Liu, X.; Peng, B.; Wong, L. M.; Sum, T. C.; Wang, S.; Xiong, Q. Composition-Tunable Vertically Aligned CdS_xSe_{1-x} Nanowire Arrays *via* van der Waals Epitaxy: Investigation of Optical Properties and Photocatalytic Behavior. *Adv. Mater.* **2012**, *24*, 4151–4156.
42. Yang, C.; Zhou, B.; Miao, S.; Yang, C.; Cai, B.; Zhang, W.-H.; Xu, X. $Cu_2Ge(S_{3-x}Se_x)$ Colloidal Nanocrystals: Synthesis, Characterization, and Composition-Dependent Band Gap Engineering. *J. Am. Chem. Soc.* **2013**, *135*, 5958–5961.
43. Fan, F.-J.; Wu, L.; Gong, M.; Liu, G.; Wang, Y.-X.; Yu, S.-H.; Chen, S.; Wang, L.-W.; Gong, X.-G. Composition- and Band-Gap-Tunable Synthesis of Wurtzite-Derived $Cu_2ZnSn(S_{1-x}Se_x)_4$ Nanocrystals: Theoretical and Experimental Insights. *ACS Nano* **2013**, *7*, 1454–1463.
44. Liu, M.-L.; Chen, I.-W.; Huang, F.-Q.; Chen, L.-D. Improved Thermoelectric Properties of Cu-Doped Quaternary Chalcogenides of $Cu_2CdSnSe_4$. *Adv. Mater.* **2009**, *21*, 3808–3812.
45. Matsushita, H.; Maeda, T.; Katsui, A.; Takizawa, T. Thermal Analysis and Synthesis from the Melts of Cu-Based Quaternary Compounds Cu–III–IV–VI_4 and Cu_2–II–IV–VI_4 (II=Zn,Cd; III=Ga,In; IV=Ge,Sn; VI=Se). *J. Cryst. Growth* **2000**, *208*, 416–422.
46. Ibáñez, M.; Cadavid, D.; Zamani, R.; García-Castelló, N.; Izquierdo-Roca, V.; Li, W.; Fairbrother, A.; Prades, J. D.; Shavel, A.; Arbiol, J.; *et al*. Composition Control and Thermoelectric Properties of Quaternary Chalcogenide Nanocrystals: The Case of Stannite $Cu_2CdSnSe_4$. *Chem. Mater.* **2012**, *24*, 562–570.
47. Wang, D.; Wan, L.; Bai, Z.; Cao, Y. Mixed Phases in *p*-Type $CuInSe_2$ Thin Films Detected by Using Micro-Raman Scattering Spectroscopy. *Appl. Phys. Lett.* **2008**, *92*, 211912.
48. Wang, D.; Lieber, C. M. Inorganic Materials: Nanocrystals Branch Out. *Nat. Mater.* **2003**, *2*, 355–356.
49. Qi, W.; de Graaf, J.; Qiao, F.; Marras, S.; Manna, L.; Dijkstra, M. Ordered Two-Dimensional Superstructures of Colloidal Octapod-Shaped Nanocrystals on Flat Substrates. *Nano Lett.* **2012**, *12*, 5299–5303.
50. Ibáñez, M.; Zamani, R.; Li, W.; Shavel, A.; Arbiol, J.; Morante, J. R.; Cabot, A. Extending the Nanocrystal Synthesis Control to Quaternary Compositions. *Cryst. Growth. Des.* **2012**, *12*, 1085–1090.
51. Schuster, F.; Furtmayr, F.; Zamani, R.; Magn, C.; Morante, J. R.; Arbiol, J.; Garrido, J. A.; Stutzmann, M. Self-Assembled GaN Nanowires on Diamond. *Nano Lett.* **2012**, *12*, 2199–2204.
52. Arbiol, J.; Magén, C.; Becker, P.; Jacopin, G.; Chernikov, A.; Schafer, S.; Furtmayr, F.; Tchernycheva, M.; Rigutti, L.; Teubert, J.; *et al*. Self-Assembled GaN Quantum Wires on GaN/AlN Nanowire Templates. *Nanoscale* **2012**, *4*, 7517–7524.
53. http://departments.icmab.es/gaen/research/222.

54. Carbone, L.; Kudera, S.; Carlino, E.; Parak, W. J.; Giannini, C.; Cingolani, R.; Manna, L. Multiple Wurtzite Twinning in CdTe Nanocrystals Induced by Methylphosphonic Acid. *J. Am. Chem. Soc.* **2006**, *128*, 748–755.
55. Zhukov, E. G.; Mkrtchyan, S. A.; Davletov, K. O.; Kalinnikov, V. T.; Ashirov, O. A. The $CdSe-Cu_2SnSe_3$ System. *Russ. J. Inorg. Chem.* **1982**, *27*, 426–427.
56. Grillo, V.; Rossi, F. STEM_CELL: A Software Tool for Electron Microscopy. Part 2—Analysis of Crystalline Materials. *Ultramicroscopy* **2013**, *125*, 112–129.
57. Nakamura, S.; Maeda, T.; Wada, T. Phase Stability and Electronic Structure of In-Free Photovoltaic Materials $Cu_2IISnSe_4$ (II: Zn, Cd, Hg). *Jpn. J. Appl. Phys.* **2011**, *50*, 05FF01.
58. Luther, J. M.; Jain, P. K.; Ewers, T.; Alivisatos, A. P. Localized Surface Plasmon Resonances Arising from Free Carriers in Doped Quantum Dots. *Nat. Mater.* **2011**, *10*, 361–366.
59. Li, W.; Zamani, R.; Ibáñez, M.; Cadavid, D.; Shavel, A.; Morante, J. R.; Arbiol, J.; Cabot, A. Metal Ions To Control the Morphology of Semiconductor Nanoparticles: Copper Selenide Nanocubes. *J. Am. Chem. Soc.* **2013**, *135*, 4664–4667.
60. Li, W.; Zamani, R.; Rivera Gil, P.; Pelaz, B.; Ibáñez, M.; Cadavid, D.; Shavel, A.; Alvarez-Puebla, R. A.; Parak, W. J.; Arbiol, J.; *et al*. CuTe Nanocrystals: Shape and Size Control, Plasmonic Properties, and Use as SERS Probes and Photothermal Agents. *J. Am. Chem. Soc.* **2013**, *135*, 7098–7101.
61. Kriegel, I.; Jiang, C.; Rodríguez-Fernández, J.; Schaller, R. D.; Talapin, D. V.; da Como, E.; Feldmann, J. Tuning the Excitonic and Plasmonic Properties of Copper Chalcogenide Nanocrystals. *J. Am. Chem. Soc.* **2012**, *134*, 1583–1590.
62. Dorfs, D.; Härtling, T.; Miszta, K.; Bigall, N. C.; Kim, M. R.; Genovese, A.; Falqui, A.; Povia, M.; Manna, L. Reversible Tunability of the Near-Infrared Valence Band Plasmon Resonance in $Cu_{2-x}Se$ Nanocrystals. *J. Am. Chem. Soc.* **2011**, *133*, 11175–11180.
63. Alvarez-Puebla, R. A.; Liz-Marzán, L. M. Traps and Cages for Universal SERS Detection. *Chem. Soc. Rev.* **2012**, *41*, 43–51.
64. Alvarez-Puebla, R. A.; Liz-Marzán, L. M. SERS Detection of Small Inorganic Molecules and Ions. *Angew. Chem., Int. Ed.* **2012**, *51*, 11214–11223.
65. Okunishi, E.; Ishikawa, I.; Sawada, H.; Hosokawa, F.; Hori, M.; Kondo, Y. Visualization of Light Elements at Ultrahigh Resolution by STEM Annular Bright Field Microscopy. *Microsc. Microanal.* **2009**, *15*, 164–165.
66. Findlay, S.; Azuma, S.; Shibata, N.; Okunishi, E.; Ikuhara, Y. Direct Oxygen Imaging within a Ceramic Interface, with Some Observations upon the Dark Contrast at the Grain Boundary. *Ultramicroscopy* **2011**, *111*, 285–289.
67. Findlay, S.; Shibata, N.; Sawada, H.; Okunishi, E.; Kondo, Y.; Ikuhara, Y. Dynamics of Annular Bright Field Imaging in Scanning Transmission Electron Microscopy. *Ultramicroscopy* **2010**, *110*, 903–923.
68. Ishikawa, R.; Okunishi, E.; Sawada, H.; Kondo, Y.; Hosokawa, F.; Abe, E. Direct Imaging of Hydrogen-Atom Columns in a Crystal by Annular Bright-Field Electron Microscopy. *Nat. Mater.* **2011**, *10*, 278–281.
69. Bar-Sadan, M.; Barthel, J.; Shtrikman, H.; Houben, L. Direct Imaging of Single Au Atoms within GaAs Nanowires. *Nano Lett.* **2012**, *12*, 2352–2356.
70. Bernal, S.; Botana, F. J.; Calvino, J. J.; López-Cartes, C.; Pérez-Omil, J. A.; Rodríguez-Izquierdo, J. M. The Interpretation of {HREM} Images of Supported Metal Catalysts Using Image Simulation: Profile View Images. *Ultramicroscopy* **1998**, *72*, 135–164.
71. Grillo, V.; Rotunno, E. STEM_CELL: A Software Tool for Electron Microscopy: Part I—Simulations. *Ultramicroscopy* **2013**, *125*, 97–111.
72. Soler, J. M.; Artacho, E.; Gale, J. D.; García, A.; Junquera, J.; Ordejón, P.; Sánchez-Portal, D. The SIESTA Method for textitab initio Order-N Materials Simulation. *J. Phys.: Condens. Matter* **2002**, *14*, 2745.
73. Ordejón, P.; Artacho, E.; Soler, J. M. Self-Consistent Order-*N* Density-Functional Calculations for Very Large Systems. *Phys. Rev. B* **1996**, *53*, R10441–R10444.
74. Troullier, N.; Martins, J. L. Efficient Pseudopotentials for Plane-Wave Calculations. II. Operators for Fast Iterative Diagonalization. *Phys. Rev. B* **1991**, *43*, 8861–8869.
75. Ceperley, D. M.; Alder, B. J. Ground State of the Electron Gas by a Stochastic Method. *Phys. Rev. Lett.* **1980**, *45*, 566–569.
76. Perdew, J. P.; Zunger, A. Self-Interaction Correction to Density-Functional Approximations for Many-Electron Systems. *Phys. Rev. B* **1981**, *23*, 5048–5079.